JACS
JOURNAL OF THE AMERICAN CHEMICAL SOCIETY

Tailoring Local Chemical Ordering via Elemental Tuning in High-Entropy Alloys

Zhennan Huang,[‖] Tangyuan Li,[‖] Boyang Li,[‖] Qi Dong, Jacob Smith, Shuke Li, Lin Xu, Guofeng Wang,* Miaofang Chi,* and Liangbing Hu*

Cite This: *J. Am. Chem. Soc.* 2024, 146, 2167−2173

Read Online

ACCESS | Metrics & More | Article Recommendations | Supporting Information

ABSTRACT: Due to the large multi-elemental space desired for property screening and optimization, high-entropy alloys (HEAs) hold greater potential over conventional alloys for a range of applications, such as structural materials, energy conversion, and catalysis. However, the relationship between the HEA composition and its local structural/elemental configuration is not well understood, particularly in noble-metal-based HEA nanomaterials, hindering the design and development of nano-HEAs in energy conversion and catalysis applications. Herein, we determined precise atomic-level structural and elemental arrangements in model HEAs composed of RhPtPdFeCo and RuPtPdFeCo to unveil their local characteristics. Notably, by changing just one constituent element in the HEA (Rh to Ru), we found dramatic changes in the elemental arrangement from complete random mixing to a local single elemental ordering feature. Additionally, we demonstrate that the local ordering in RuPtPdFeCo can be further controlled by varying the Ru concentration, allowing us to toggle between local Ru clustering and distinct heterostructures in multicomponent systems. Overall, our study presents a practical approach for manipulating local atomic structures and elemental arrangements in noble-metal-based HEA systems, which could provide in-depth knowledge to mechanistically understand the functionality of noble-metal-based HEA nanomaterials in practical applications.

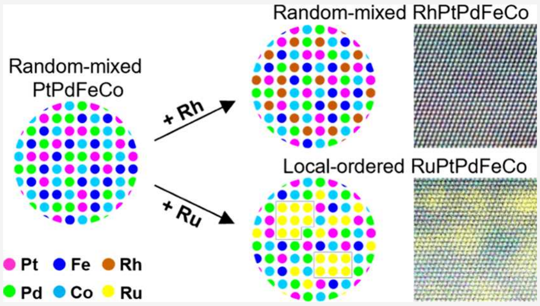

■ INTRODUCTION

High-entropy alloys (HEAs) represent a vast category of multicomponent materials that typically contain four or more principal elements with close atomic ratios.[1,2] Compared to conventional unary or simple alloys, HEAs demonstrate superior performance in a range of applications, including as structural and engineering materials[3−7] as well as energy storage/conversion[8−11] and catalysis.[12−16] Notably, HEAs provide an unprecedentedly large material space[17] in which different properties and behaviors can be achieved via unique structural and chemical transformations[18−20] induced by changing the multi-elemental composition.[4,21,22] For example, enhanced mechanical and physical properties have been observed by introducing secondary phases,[3] local oxidation,[23] and short-range orderings[24−27] in HEAs via compositional design. Despite notable successes, the development of these compositionally complex alloys with localized features has primarily focused on bulk materials for structural and engineering purposes[7,28−30] centered around cost-effective, non-noble elements. There is a lack of systematic investigation of the local structural and chemical characteristics of HEAs suitable for energy conversion and catalytic purposes such as the noble-metal-based HEA nanomaterials. To better design HEA catalysts, it is necessary to assess their fine structures as the composition changes and to establish a deeper understanding of the composition−structure relationships in these multicomponent systems.

Herein, we investigate how elemental composition can induce changes to the local structure and elemental orderings in noble-metal-based HEA nanoparticles (NPs) at the atomic level. A PtPdFeCoM (M = Rh, Ru) multicomponent HEA was selected as a model system as it features elements commonly employed in energy conversion and catalytic applications.[31−38] Using a combination of high-angle annular dark field scanning transmission electron microscopy (HAADF-STEM) and STEM-based energy dispersive X-ray spectroscopy (STEM-EDS), we resolved the atomistic configurations of RhPtPdFeCo and RuPtPdFeCo and observed distinct changes in the local elemental arrangements by varying just one constituent (Rh → Ru) in the HEA systems. As illustrated in Figure 1, the introduction of Rh in PtPdFeCo results in a well-mixed solid solution structure. In contrast, the use of Ru leads to localized features of cluster-level Ru aggregates distributed in the

Received: October 28, 2023
Revised: December 21, 2023
Accepted: December 26, 2023
Published: January 12, 2024

https://doi.org/10.1021/jacs.3c12048
J. Am. Chem. Soc. 2024, 146, 2167−2173

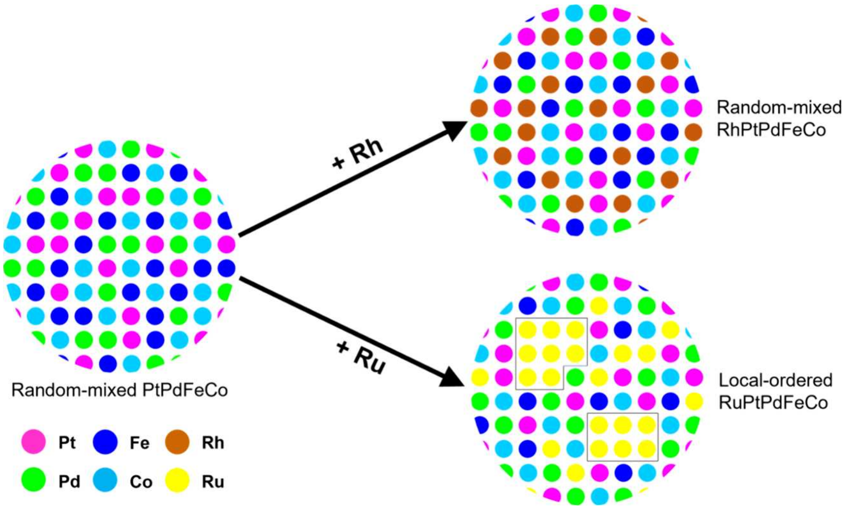

Figure 1. Composition−structure relationship in HEAs with one constituent difference. When Rh is added to PtPdFeCo, it leads to the formation of random elemental mixing of RhPtPdFeCo HEA structures. In contrast, substituting Rh with Ru promotes the formation of localized Ru aggregation, resulting in the cluster-level ordering of Ru in the PtPdFeCo solid solution, while still maintaining a single-phase crystal structure.

uniformly mixed Pt, Pd, Fe, and Co solid-solution matrix. Additionally, we find that varying the concentration of Ru within the RuPtPdFeCo system modifies the local ordering and alters the segregated structure significantly, allowing us to toggle between segregated Ru clusters and Ru cluster networks in the HEA matrix and produce Ru-PtPdFeCo multicomponent heterostructures. First-principles density functional theory (DFT) calculations suggest that the formation enthalpy varies substantially with the elemental substitution (Rh → Ru), resulting in a large difference in the Gibbs free energy of the multicomponent systems, which favors the formation of ordered or disordered structures in the HEAs. This study, combining atomistic characterization with DFT calculations, presents an in-depth understanding of the complex composition−structure relationships in noble-metal-based HEAs, providing guidance for the design and development of HEA catalysts through local structure and chemistry manipulation.

■ RESULTS AND DISCUSSION

We first synthesized RhPtPdFeCo NPs using a thermal shock approach that has been previously demonstrated for the fabrication of nanoscale HEAs[39] (see the Experimental Methods in the Supporting Information for details). The elemental precursor salts were applied at equal molar ratios to achieve ∼20 atom % Rh in the multicomponent systems (denoted as 20RhPtPdFeCo). The resulting 20RhPtPdFeCo NPs were ∼20 nm in size, as characterized by HAADF-STEM (Figure S1). High-resolution STEM-EDS mapping also showed that the Rh, Pt, Pd, Fe, and Co were uniformly dispersed throughout the 20RhPtPdFeCo NPs (Figure 2a and Figure S1a), indicating the successful mixing of all the elements in the NPs. We also analyzed the crystal structures of the NPs using high-resolution HAADF-STEM imaging. As shown in Figure 2b, the 20RhPtPdFeCo demonstrates a closely packed structure at the atomic level with an interplanar distance of 2.23 Å, matching well with the {111} planes of the face-centered cubic (FCC) structure. The corresponding atomistic EDS maps depict the distribution of the five constituent elements at all-atom column positions. Only minor intensity fluctuations appear in the EDS line scan profiles (Figure S2a), suggesting a consistent distribution of all the elements within the NPs. As such, we conclude that 20RhPtPdFeCo features a uniform elemental distribution within a single FCC crystal structure.

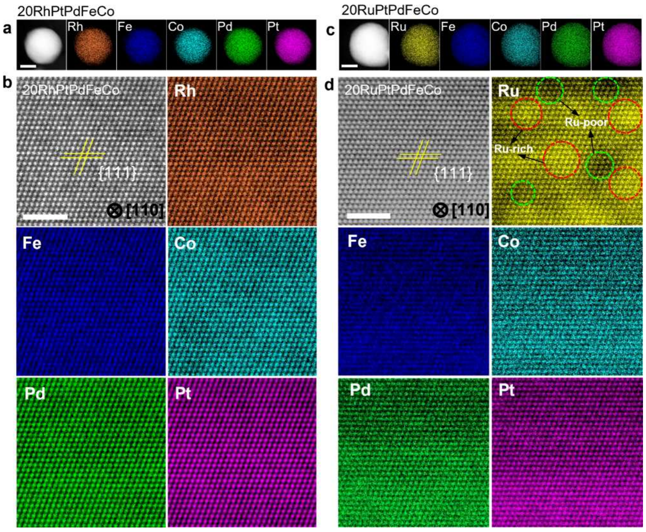

Figure 2. STEM imaging and elemental mapping of 20RhPtPdFeCo and 20RuPtPdFeCo. (a) HAADF-STEM and STEM-EDS maps of a typical 20RhPtPdFeCo NP, demonstrating a uniform elemental distribution. Scale bar = 10 nm. (b) The 20RhPtPdFeCo NP shows an FCC crystal structure, and the corresponding elemental maps of Rh, Pt, Pd, Fe, and Co demonstrate uniform elemental mixing at all atom locations. Scale bar = 2 nm. (c) HAADF-STEM and STEM-EDS maps of a typical 20RuPtPdFeCo NP with a uniform elemental distribution. Scale bar = 10 nm. (d) The 20RuPtPdFeCo also exhibits an FCC crystal structure down to the atomistic scale. However, the elemental arrangement of Ru shows obvious variations throughout the mapping area in stark contrast to Pt, Pd, Fe, and Co. Local enrichment and deficiency areas of Ru are marked by red and green circles in the Ru map, respectively. Scale bar = 2 nm.

We also synthesized 20RuPtPdFeCo HEA NPs under the same conditions as a comparison to 20RhPtPdFeCo to better understand how changing the elemental composition (Ru replacing Rh) influences the alloy's local structure. Ru and Rh are both significant noble metals in the field of catalysis,[40] and they share a similar atomic radius and electronegativity.

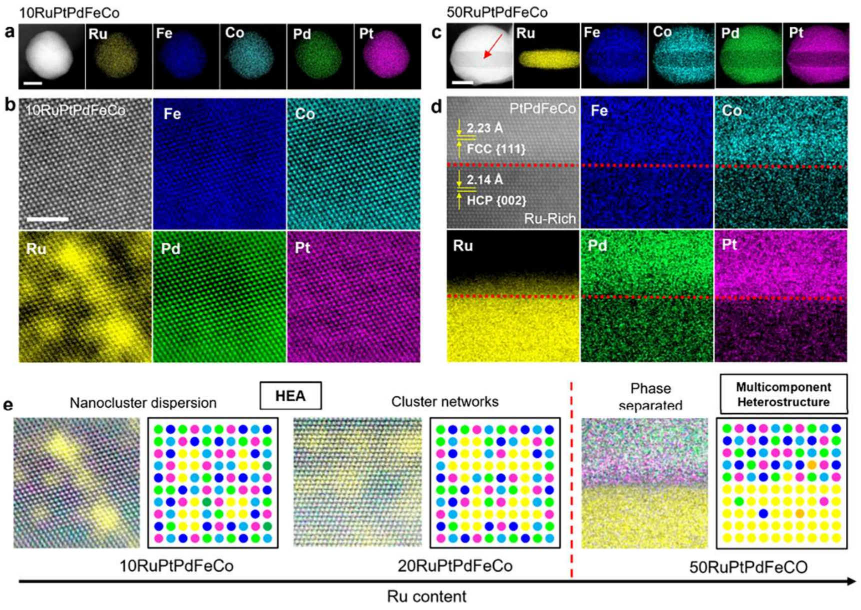

Figure 3. Composition−structure relationships in the RuPtPdFeCo system. (a) STEM imaging and STEM-EDS mapping of a 10RuPtPdFeCo NP (scale bar = 10 nm). (b) Atomistic STEM analysis of the 10RuPtPdFeCo, indicating the presence of segregated Ru clusters in single-phase HEA (Scale bar = 2 nm). (c) STEM imaging and STEM-EDS mapping of a 50RuPtPdFeCo NP (Scale bar = 10 nm). (d) Atomistic STEM analysis of the 50RuPtPdFeCo, indicating the presence of Ru-PtPdFeCo heterostructures. The interface of the heterostructure is marked by the red dashed line (Scale bar = 2 nm). Composition−structure relationships of the RuPtPdFeCo NPs as a function of the Ru content. EDS overlay images of Ru, Pt, Pd, Fe, and Co and corresponding schematics at Ru concentrations of 10, 20, and 50 at. % in the quinary RuPtPdFeCo system.

Elemental analysis of the 20RuPtPdFeCo HEA NPs shows that Ru, Pt, Pd, Fe, and Co are homogeneously distributed within the NPs with no obvious elemental segregation (Figure 2c and Figure S1b). Fast Fourier transform (FFT) analysis shows that the crystal structure of 20RuPtPdFeCo is also FCC (Figure S3) with the *d* spacing of the intersected planes measured to be 2.23 Å (Figure 2d), corresponding to the FCC {111} planes. Therefore, the long-range compositional homogeneity and single-phase FCC crystal structure remains unchanged when substituting Rh with Ru in this quinary system. However, atomic mapping unveils an unexpected elemental ordering in the 20RuPtPdFeCo sample, in which the Ru atoms exhibit localized segregation in the NPs. As demonstrated in Figure 2d, there is an obvious elemental agglomeration phenomenon in the Ru map, where Ru-rich and Ru-poor regions are designated by red and green circles, respectively. The corresponding EDS line scan profile illustrates a significant fluctuation of Ru signals at various positions, while the remaining four constituent elements exhibit a relatively constant intensity across the mapping region (Figure S2b). The Ru aggregates are a few atoms in length, resembling cluster-sized agglomerations in the multicomponent system. Taken together, we conclude that 20RuPtPdFeCo features an FCC structure with the presence of localized Ru clustering in the solid solution PtPdFeCo, demonstrating the impact that the elemental composition can have on the local arrangements in noble-metal system HEAs.

Due to the limited solubility of Ru in the PtPdFeCo matrix, we next explored the effect of the Ru loading (atom %) in the quinary system on the local atomic arrangements to gain more mechanistic understanding on the composition−structure relationship. We synthesized two additional quinary systems with Ru loadings of 10 and 50 at. % (denoted as 10RuPtPdFeCo and 50RuPtPdFeCo, respectively) by changing the dosage of the Ru precursor during synthesis (see the Experimental Methods in the Supporting Information for details). The elements were well mixed at the particle level in the 10RuPtPdFeCo sample (Figure 3a). Additionally, the atomic arrangement retained an FCC structure as well as clustering of Ru and high uniformity of the remaining elements (Figure 3b), which is similar to the 20RuPtPdFeCo sample. However, the lower Ru content resulted in smaller Ru clusters widely spread throughout the entire imaging region (Figure 3b) compared with the equimolar 20RuPtPdFeCo (Figure 2d). No secondary phases were observed from FFT analysis (Figure S4) of the HAADF-STEM results, confirming that the Ru clusters dispersed throughout the PtPdFeCo solid solution matrix do not alter the FCC crystal structure. In contrast, increasing the Ru content (50RuPtPdFeCo) resulted in a phase-separated heterostructure, which is distinct from the 10 and 20 atom % Ru samples. As shown in the HAADF-STEM image (Figure 3c), a sandwiched structure in the NP (red arrow) can be seen in the 50RuPtPdFeCo. The corresponding elemental maps suggest that Ru nucleated and grew independently from the other four elements and aggregated in the middle of the particle, whereas the Pt, Pd, Fe, and Co were well-distributed in the rest of the particle. As a result, a Ru-PtPdFeCo heterostructure was formed.

To better understand this multicomponent heterostructure, we conducted an atomistic structural analysis on the interface region of the 50RuPtPdFeCo sample using STEM imaging. As shown in Figure 3d, the interface is tightly packed with separated PtPdFeCo and Ru crystal regions from the high-resolution HAADF imaging and elemental mapping analysis with distinct structural characteristics (red dashed lines). Especially, the PtPdFeCo exhibits an FCC structure oriented at the [110] direction, as shown by the corresponding FFT analysis ($d_{\mathrm{FCC}\ \{111\}}$ = 2.24 Å and $d_{\mathrm{FCC}\ \{200\}}$ = 1.92 Å) in Figure S5a, which is consistent with the previous quinary 20RuPtPdFeCo structure. In comparison, the Ru region

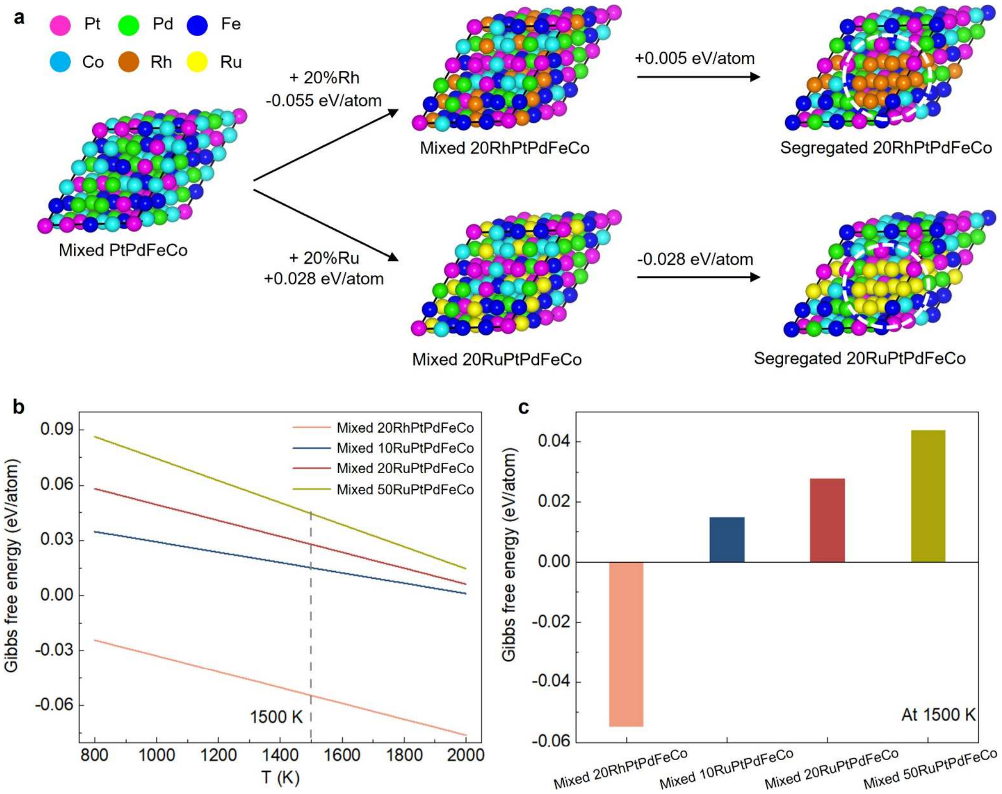

Figure 4. (a) Atomic structure and free energy changes in well mixed and locally segregated 20RuPtPdFeCo and 20RhPtPdFeCo systems. (b) Calculated linear relationship between the Gibbs free energy and temperature for mixed 10RuPtPdFeCo, mixed 20RuPtPdFeCo, mixed 50RuPtPdFeCo, and mixed 20RhPtPdFeCo. (c) Calculated free energy change of the multi-elemental systems at 1500 K.

demonstrates atomic configurations distinct from the FCC characteristics. The interplanar distances were measured to be 2.05, 2.14, and 2.33 Å, corresponding to {101}, {002}, and {100} planes of hexagonal close-packed (HCP) Ru viewed along the [110] zone axis (Figure S5b). Therefore, the Ru-rich phase undergoes a transition from the FCC in the HEA NP to the separated HCP structure, which is a thermodynamically more stable crystal structure for Ru.[41,42] Meanwhile, the tightly bonded interface is constructed with {111} FCC-PtPdFeCo and {002} HCP-Ru planes (Figure 3d), resembling an epitaxially grown multi-elemental heterostructure.[43,44]

The structural evolution of the multimetallic RuPtPdFeCo as a function of the Ru content is summarized and illustrated in Figure 3e. The quinary NPs with Ru content ranging from 10 to 20 and 50 at. % exhibit distinct features, showcasing the dispersion of segregated Ru clusters and Ru cluster networks in the HEA matrix and a Ru-multicomponent heterostructure, respectively. Those local structures in the multi-elemental NPs may provide unique properties compared to their completely random mixing status. For example, the introduction of inhomogeneous elemental distributions in HEAs could modify the local strain fields. As shown by the strain maps in Figure S6 obtained through the geometric phase analysis, the 20RuPtPdFeCo presents a substantial tensile and compressive strain randomly distributed at the atomic level, whereas the 20RhPtPdFeCo sample shows a milder strain field distribution. Such a strain in the NPs may have the potential to influence the electronic structures of the HEAs, affecting the adsorption behavior of chemical species on the NPs and subsequently modifying their catalytic performance.[45] Future studies with a careful selection of various application scenarios and reactions are crucial to systematically evaluating the difference in performance between the randomly mixed and local chemically ordered noble-metal-based HEAs. In turns of the phase-separated multimetallic heterostructures, which might form through epitaxial nucleation[46,47] in the multicomponent NPs, these heterometallic structures could function as plasmonic architectures, integrating the properties of adjacent domains to access distinct behaviors in optoelectronics and catalysis.[48,49] The heterometallic interfaces could also serve to modulate the interfacial electric field, suggesting potential in electrochemistry.[50] Therefore, tuning the content of a single constituent with limited solubility in the HEA solid solutions suggests a feasible route for designing and developing multimetallic nanostructures with advantages across various applications.

We also performed first-principles density functional theory (DFT) calculations to study the influence of chemical composition on the phases (mixed vs segregated) within different multielement alloy systems. Based on experimental observations, atomic models of homogeneously mixed PtPdFeCo, 20RhPtPdFeCo, and 20RuPtPdFeCo HEAs were constructed (Figure 4a). Consistent with the multicomponent alloying reaction that occurred in our experiment, we calculated the free energy change for the following reaction, assuming the alloys have a completely mixed structure:

$$0.8 \times Pt_{0.25}Pd_{0.25}Fe_{0.25}Co_{0.25} + 0.2 \times M \rightarrow Pt_{0.2}Pd_{0.2}Fe_{0.2}Co_{0.2}M_{0.2} \quad (1)$$

Here, M represents the fifth element added in the multiple element alloy system. The total energy difference between the reactants and products, that is, the enthalpy change ΔH, was obtained via DFT calculations. The ideal configurational entropy for HEAs can be calculated as

$$S = -k_B \sum x_b \times \ln(x_b) \tag{2}$$

where S is the configurational entropy, k_B is the Boltzmann constant, and x_b is the mole fraction of the component in the HEA system.

Therefore, we obtained linear relationships between the Gibbs free energy change and temperature of the multicomponent systems using the equation:

$$\Delta G = \Delta H - T\Delta S \tag{3}$$

As shown in Figure 4a and Table S1, we predicted the free energy change of reaction 1 to be −0.055 eV/atom for the 20RhPtPdFeCo system and 0.028 eV/atom for the 20RuPtPdFeCo system at 1500 K (experimental synthesis temperature). A negative value of the calculated free energy change indicates that reaction 1 is thermodynamically favorable. Consequently, we predict that the introduction of Rh into the PtPdFeCo system will lead to the formation of the uniformly mixed HEA, whereas potential phase segregation will occur when Ru is added to the PtPdFeCo system. Furthermore, we compared the calculated system energy of the PtPdFeCoM (M = Ru or Rh) alloy with a local segregation of M (Figure 4a) and found that the segregated 20RuPtPdFeCo was 0.028 eV/atom more stable than the mixed 20RuPtPdFeCo system. In contrast, the segregated 20RhPtPdFeCo structure was predicted to be 0.005 eV/atom less stable than its mixed phase (Figure 4a). These predictions further indicate that the structure of local Ru clustering is favorable in the 20RuPtPdFeCo system but not in the 20RhPtPdFeCo system, which is consistent with our STEM-EDS findings in Figure 2. The DFT results (Note S1) suggest that the chemical-affinity disparity plays a more significant role than the atomic-radius difference for the observed different local chemical ordering between the RhPtPdFeCo and RuPtPdFeCo HEAs, which is consistent with previous predictions regarding CoCuFeNiPd and CoCuFeNiTi HEAs.[51]

We also investigated how the concentration of Ru affects the phase stability of the RuPtPdFeCo system. We constructed different models of $\mathrm{Ru}_x(\mathrm{PtPdFeCo})_{1-x}$ with the molar concentration of Ru (x) to be 0.1, 0.2, and 0.5 (Figure S7). Using eq 3, we calculated the Gibbs free energies of these systems as a function of temperature (Figure 4b). The free energy changes of reaction 1 at 1500 K for the $\mathrm{Ru}_x(\mathrm{PtPdFeCo})_{1-x}$ system were calculated to be 0.015, 0.028, and 0.044 eV/atom for x equal to 0.1, 0.2, and 0.5, respectively (Figure 4c). These positive energy changes show that the RuPtPdFeCo system does not prefer a well-mixed solid solution structure; thus, a potential phase segregation phenomenon would exist in this multicomponent system. The tendency of phase segregation is also more pronounced when the concentration of Ru increases, which is in good agreement with our experimental observations (Figure 3e).

Overall, the free energy change predicted by our DFT calculations provides insight into the outcomes of introducing Rh or Ru into the PtPdFeCo system. Specifically, our predictions indicate that the inclusion of Rh lowers the formation energy of quinary RhPtPdFeCo and promotes the formation of a homogeneously mixed HEA phase. In contrast, Ru would drastically increase the energy of the system and form potential segregations in RuPtPdFeCo with various Ru concentrations.

■ CONCLUSIONS

In conclusion, we have conducted atomic-level structural and elemental characterization of noble-metal-based HEA NPs and revealed a composition−structure relationship through the fine control of one constituent element, namely, PtPdFeCoM (M = Ru/Rh). We demonstrate that the substitution of Rh to Ru in the HEA can drastically switch the local structure from homogeneous elemental mixing to single-element segregation in an overall solid solution HEA. Tuning the Ru concentration further allows us to toggle the local arrangements from a segregated Ru-cluster to a Ru-cluster network in the HEA and finally to Ru-PtPdFeCo heterostructures, accessing unique structural features compared to typical HEAs with randomly mixed solid solution structures. The predicted free energy of formation obtained from DFT calculations showed that an inversed energy difference of −0.055 and 0.028 eV/atom was calculated by introducing equimolar Rh and Ru in the PtPdFeCo system, respectively, which indicated that RhPtPdFeCo will form toward a well mixed solid solution structure, while segregations would happen in the quinary RuPtPdFeCo system. Varying the Ru concentration in the RuPtPdFeCo shows the segregation to be more predominant with the increase of the Ru proportion in the quinary system, which is consistent with our experimental findings. These insights gained by resolving the local structural and chemical configurations in HEAs at the atomic level would provide a fundamental basis and guidance toward mechanistic understanding of the role of noble-metal-based HEAs for practical reactions.

■ ASSOCIATED CONTENT

Supporting Information

The Supporting Information is available free of charge at https://pubs.acs.org/doi/10.1021/jacs.3c12048.

Experimental methods, additional HAADF-STEM images, STEM-EDS line scans and mappings, FFT analysis, geometric phase analysis, theoretical modeling, and calculation (PDF)

■ AUTHOR INFORMATION

Corresponding Authors

Guofeng Wang − *Department of Mechanical Engineering and Materials Science, University of Pittsburgh, Pittsburgh, Pennsylvania 15261, United States;* orcid.org/0000-0001-8249-4101; Email: guw8@pitt.edu

Miaofang Chi − *Center for Nanophase Materials Science, Oak Ridge National Laboratory, Oak Ridge, Tennessee 37831, United States;* orcid.org/0000-0003-0764-1567; Email: chim@ornl.gov

Liangbing Hu − *Department of Materials Science and Engineering, University of Maryland, College Park, Maryland 20742, United States;* orcid.org/0000-0002-9456-9315; Email: binghu@umd.edu

Authors

Zhennan Huang − *Department of Materials Science and Engineering, University of Maryland, College Park, Maryland 20742, United States*

Tangyuan Li − *Department of Materials Science and Engineering, University of Maryland, College Park, Maryland 20742, United States;* orcid.org/0009-0001-1232-0613

Boyang Li − *Department of Mechanical Engineering and Materials Science, University of Pittsburgh, Pittsburgh, Pennsylvania 15261, United States*

Qi Dong − *Department of Materials Science and Engineering, University of Maryland, College Park, Maryland 20742, United States*

Jacob Smith − *Center for Nanophase Materials Science, Oak Ridge National Laboratory, Oak Ridge, Tennessee 37831, United States*

Shuke Li − *Department of Materials Science and Engineering, University of Maryland, College Park, Maryland 20742, United States;* orcid.org/0000-0001-5715-9942

Lin Xu − *Department of Materials Science and Engineering, University of Maryland, College Park, Maryland 20742, United States;* orcid.org/0000-0002-3863-0214

Complete contact information is available at: https://pubs.acs.org/10.1021/jacs.3c12048

Author Contributions

‖Z. H., T. L., and B. L. contributed equally to this work.

Notes

The authors declare no competing financial interest.

■ ACKNOWLEDGMENTS

L.H. acknowledges support from the University of Maryland A. James Clark School of Engineering. Part of the Research was sponsored by the US DOE, Office of Science, Office of Basic Energy Sciences (BES), Chemical Sciences, Geosciences, and Biosciences Division, Catalysis Science program. Technique development and data analysis were supported by US DOE Office of Science under Early Career award no. ERKCZ55. Microscopy experiments were performed by the Center for Nanophase Materials Sciences (CNMS), which is a US Department of Energy, Office of Science User Facility at Oak Ridge National Laboratory. B.L. and G.W. acknowledge the financial support for this research provided by the National Science Foundation (NSF) (grant no. DMR 1905572). This research was also supported in part by the University of Pittsburgh Center for Research Computing, RRID:SCR_022735, through the computer resources provided. Specifically, this work used the H2P cluster, which is supported by NSF award no. OAC-2117681.

■ REFERENCES

(1) Yao, Y.; Dong, Q.; Brozena, A.; Luo, J.; Miao, J.; Chi, M.; Wang, C.; Kevrekidis, I. G.; Ren, Z. J.; Greeley, J.; Wang, G.; Anapolsky, A.; Hu, L. High-Entropy Nanoparticles: Synthesis-Structureproperty Relationships and Data-Driven Discovery. *Science* **2022**, *376*, No. eabn3103.

(2) Sun, Y.; Dai, S. High-Entropy Materials for Catalysis: A New Frontier. *Sci. Adv.* **2021**, *7*, 1−24.

(3) Ren, J.; Zhang, Y.; Zhao, D.; Chen, Y.; Guan, S.; Liu, Y.; Liu, L.; Peng, S.; Kong, F.; Poplawsky, J. D.; Gao, G.; Voisin, T.; An, K.; Wang, Y. M.; Xie, K. Y.; Zhu, T.; Chen, W. Strong yet Ductile Nanolamellar High-Entropy Alloys by Additive Manufacturing. *Nature* **2022**, *608*, 62−68.

(4) Ding, Q.; Zhang, Y.; Chen, X.; Fu, X.; Chen, D.; Chen, S.; Gu, L.; Wei, F.; Bei, H.; Gao, Y.; Wen, M.; Li, J.; Zhang, Z.; Zhu, T.; Ritchie, R. O.; Yu, Q. Tuning Element Distribution, Structure and Properties by Composition in High-Entropy Alloys. *Nature* **2019**, *574*, 223−227.

(5) Raabe, D.; Tasan, C. C.; Olivetti, E. A. Strategies for Improving the Sustainability of Structural Metals. *Nature* **2019**, *575*, 64−74.

(6) Gludovatz, B.; Hohenwarter, A.; Catoor, D.; Chang, E. H.; George, E. P.; Ritchie, R. O. A Fracture-Resistant High-Entropy Alloy for Cryogenic Applications. *Science* **2014**, *345*, 1153−1158.

(7) Yong, Z. *High-Entropy Materials: Advances and Applications*; CRC Press, 2023 DOI: 10.1201/9781003319986.

(8) Zhang, R.; Wang, C.; Zou, P.; Lin, R.; Ma, L.; Yin, L.; Li, T.; Xu, W.; Jia, H.; Li, Q.; Sainio, S.; Kisslinger, K.; Trask, S. E.; Ehrlich, S. N.; Yang, Y.; Kiss, A. M.; Ge, M.; Polzin, B. J.; Lee, S. J.; Xu, W.; Ren, Y.; Xin, H. L. Compositionally Complex Doping for Zero-Strain Zero-Cobalt Layered Cathodes. *Nature* **2022**, *610*, 67−73.

(9) Lun, Z.; Ouyang, B.; Kwon, D. H.; Ha, Y.; Foley, E. E.; Huang, T. Y.; Cai, Z.; Kim, H.; Balasubramanian, M.; Sun, Y.; Huang, J.; Tian, Y.; Kim, H.; McCloskey, B. D.; Yang, W.; Clément, R. J.; Ji, H.; Ceder, G. Cation-Disordered Rocksalt-Type High-Entropy Cathodes for Li-Ion Batteries. *Nat. Mater.* **2021**, *20*, 214−221.

(10) Haruna, A. B.; Onoh, E. U.; Ozoemena, K. I. Emerging High-Entropy Materials as Electrocatalysts for Rechargeable Zinc−Air Batteries. *Curr. Opin. Electrochem.* **2023**, *39*, 2451−9103.

(11) Batchelor, T. A. A.; Pedersen, J. K.; Winther, S. H.; Castelli, I. E.; Jacobsen, K. W.; Rossmeisl, J. High-Entropy Alloys as a Discovery Platform for Electrocatalysis. *Joule* **2019**, *3*, 834−845.

(12) Yao, Y.; Huang, Z.; Li, T.; Wang, H.; Liu, Y.; Stein, H. S.; Mao, Y.; Gao, J.; Jiao, M.; Dong, Q.; et al. High-Throughput, Combinatorial Synthesis of Multimetallic Nanoclusters. *Proc. Natl. Acad. Sci. U. S. A.* **2020**, *117*, 6316−6322.

(13) Li, T.; Dong, Q.; Huang, Z.; Wu, L.; Yao, Y.; Gao, J.; Wang, X.; Zhang, H.; Wang, D.; Li, T.; et al. Interface Engineering between Multi-Elemental Alloy Nanoparticles and a Carbon Support toward Stable Catalysts. *Adv. Mater.* **2022**, *34*, 2106436.

(14) Cao, G.; Liang, J.; Guo, Z.; Yang, K.; Wang, G.; Wang, H.; Wan, X.; Li, Z.; Bai, Y.; Zhang, Y.; Liu, J.; Feng, Y.; Zheng, Z.; Lu, C.; He, G.; Xiong, Z.; Liu, Z.; Chen, S.; Guo, Y.; Zeng, M.; Lin, J.; Fu, L. Liquid Metal for High-Entropy Alloy Nanoparticles Synthesis. *Nature* **2023**, *619*, 73−77.

(15) Plenge, M. K.; Pedersen, J. K.; Mints, V. A.; Arenz, M.; Rossmeisl, J. Following Paths of Maximum Catalytic Activity in the Composition Space of High-Entropy Alloys. *Adv. Energy Mater.* **2023**, *13*, 2202962.

(16) Batchelor, T. A. A.; Löffler, T.; Xiao, B.; Krysiak, O. A.; Strotkötter, V.; Pedersen, J. K.; Clausen, C. M.; Savan, A.; Li, Y.; Schuhmann, W.; Rossmeisl, J.; Ludwig, A. Complex-Solid-Solution Electrocatalyst Discovery by Computational Prediction and High-Throughput Experimentation**. *Angew. Chem., Int. Ed.* **2021**, *60*, 6932−6937.

(17) Banko, L.; Tetteh, E. B.; Kostka, A.; Piotrowiak, T. H.; Krysiak, O. A.; Hagemann, U.; Andronescu, C.; Schuhmann, W.; Ludwig, A. Microscale Combinatorial Libraries for the Discovery of High-Entropy Materials. *Adv. Mater.* **2023**, *35*, 2207635.

(18) Morris, D.; Yao, Y.; Finfrock, Y. Z.; Huang, Z.; Shahbazian-Yassar, R.; Hu, L.; Zhang, P. Composition-Dependent Structure and Properties of 5- and 15-Element High-Entropy Alloy Nanoparticles. *Cell Reports Physical Science* **2021**, *2*, No. 100641.

(19) Yao, Y.; Huang, Z.; Hughes, L. A.; Gao, J.; Li, T.; Morris, D.; Zeltmann, S. E.; Savitzky, B. H.; Ophus, C.; Finfrock, Y. Z.; Dong, Q.; Jiao, M.; Mao, Y.; Chi, M.; Zhang, P.; Li, J.; Minor, A. M.; Shahbazian-Yassar, R.; Hu, L. Extreme Mixing in Nanoscale Transition Metal Alloys. *Matter* **2021**, *4*, 2340−2353.

(20) Yang, Y.; Zhou, J.; Zhu, F.; Yuan, Y.; Chang, D. J.; Kim, D. S.; Pham, M.; Rana, A.; Tian, X.; Yao, Y.; Osher, S. J.; Schmid, A. K.; Hu, L.; Ercius, P.; Miao, J. Determining the Three-Dimensional Atomic Structure of an Amorphous Solid. *Nature* **2021**, *592*, 60−64.

(21) Manjón, A. G.; Löffler, T.; Meischein, M.; Meyer, H.; Lim, J.; Strotkötter, V.; Schuhmann, W.; Ludwig, A.; Scheu, C. Sputter Deposition of Highly Active Complex Solid Solution Electrocatalysts into an Ionic Liquid Library: Effect of Structure and Composition on Oxygen Reduction Activity. *Nanoscale* **2020**, *12*, 23570−23577.

(22) Löffler, T.; Savan, A.; Meyer, H.; Meischein, M.; Strotkötter, V.; Ludwig, A.; Schuhmann, W. Design of Complex Solid-Solution Electrocatalysts by Correlating Configuration, Adsorption Energy Distribution Patterns, and Activity Curves. *Angew. Chem., Int. Ed.* **2020**, *59*, 5844−5850.

(23) Lei, Z.; Liu, X.; Wu, Y.; Wang, H.; Jiang, S.; Wang, S.; Hui, X.; Wu, Y.; Gault, B.; Kontis, P.; Raabe, D.; Gu, L.; Zhang, Q.; Chen, H.; Wang, H.; Liu, J.; An, K.; Zeng, Q.; Nieh, T. G.; Lu, Z. Enhanced Strength and Ductility in a High-Entropy Alloy via Ordered Oxygen Complexes. *Nature* **2018**, *563*, 546−550.

(24) Seol, J. B.; Ko, W.-S.; Sohn, S. S.; Na, M. Y.; Chang, H. J.; Heo, Y.-U.; Kim, J. G.; Sung, H.; Li, Z.; Pereloma, E.; Kim, H. S. Mechanically Derived Short-Range Order and Its Impact on the Multi-Principal-Element Alloys. *Nat. Commun.* **2022**, *13*, 1−13.

(25) Yan, X.; Zhang, Y. Functional Properties and Promising Applications of High Entropy Alloys. *Scripta Materialia* **2020**, *187*, 188−193.

(26) Chen, S.; Aitken, Z. H.; Pattamatta, S.; Wu, Z.; Yu, Z. G.; Srolovitz, D. J.; Liaw, P. K.; Zhang, Y.-W. Simultaneously Enhancing the Ultimate Strength and Ductility of High-Entropy Alloys via Short-Range Ordering. *Nat. Commun.* **2021**, *12*, 4953.

(27) Chen, S.; Wang, T.; Li, X.; Cheng, Y.; Zhang, G.; Gao, H. Short-Range Ordering and Its Impact on Thermodynamic Property of High-Entropy Alloys. *Acta Mater.* **2022**, *238*, No. 118201.

(28) Chen, X.; Wang, Q.; Cheng, Z.; Zhu, M.; Zhou, H.; Jiang, P.; Zhou, L.; Xue, Q.; Yuan, F.; Zhu, J.; Wu, X.; Ma, E. Direct Observation of Chemical Short-Range Order in a Medium-Entropy Alloy. *Nature* **2021**, *592*, 712−716.

(29) Zhang, R.; Zhao, S.; Ding, J.; Chong, Y.; Jia, T.; Ophus, C.; Asta, M.; Ritchie, R. O.; Minor, A. M. Short-Range Order and Its Impact on the CrCoNi Medium-Entropy Alloy. *Nature* **2020**, *581*, 283−287.

(30) Zhang, F. X.; Zhao, S.; Jin, K.; Xue, H.; Velisa, G.; Bei, H.; Huang, R.; Ko, J. Y. P.; Pagan, D. C.; Neuefeind, J. C.; Weber, W. J.; Zhang, Y. Local Structure and Short-Range Order in a NiCoCr Solid Solution Alloy. *Phys. Rev. Lett.* **2017**, *118*, No. 205501.

(31) Ghanekar, P.; Kubal, J.; Cui, Y.; Mitchell, G.; Delgass, W. N.; Ribeiro, F.; Greeley, J. Catalysis at Metal/Oxide Interfaces: Density Functional Theory and Microkinetic Modeling of Water Gas Shift at Pt/MgO Boundaries. *Top. Catal.* **2020**, *63*, 673−687.

(32) Li, Q.; Zhu, H.; Chen, X.; Liu, H.; Ren, Y.; Chen, Y.; Ohara, K.; Zhou, L.; Chen, J.; Deng, J.; Miao, J.; Lin, K.; Kuang, X.; Xing, X. Local Structure Insight into Hydrogen Evolution Reaction with Bimetal Nanocatalysts. *J. Am. Chem. Soc.* **2022**, *144*, 20298−20305.

(33) Li, X.; Shen, P.; Luo, Y.; Li, Y.; Guo, Y.; Zhang, H.; Chu, K. PdFe Single-Atom Alloy Metallene for N $_2$ Electroreduction. *Angew. Chem., Int. Ed.* **2022**, *134*, e202205923.

(34) Hong, J.; Hyun, S.; Tsipoaka, M.; Samdani, J. S.; Shanmugam, S. RuFe Alloy Nanoparticle-Supported Mesoporous Carbon: Efficient Bifunctional Catalyst for Li-O2and Zn-Air Batteries. *ACS Catal.* **2022**, *12*, 1718−1731.

(35) Ro, I.; Qi, J.; Lee, S.; Xu, M.; Yan, X.; Xie, Z.; Zakem, G.; Morales, A.; Chen, J. G.; Pan, X.; Vlachos, D. G.; Caratzoulas, S.; Christopher, P. Bifunctional Hydroformylation on Heterogeneous Rh-WOx Pair Site Catalysts. *Nature* **2022**, *609*, 287−292.

(36) Zeng, Y.; Liang, J.; Li, C.; Qiao, Z.; Li, B.; Hwang, S.; Kariuki, N. N.; Chang, C. W.; Wang, M.; Lyons, M.; Lee, S.; Feng, Z.; Wang, G.; Xie, J.; Cullen, D. A.; Myers, D. J.; Wu, G. Regulating Catalytic Properties and Thermal Stability of Pt and PtCo Intermetallic Fuel-Cell Catalysts via Strong Coupling Effects between Single-Metal Site-Rich Carbon and Pt. *J. Am. Chem. Soc.* **2023**, *145*, 17643−17655.

(37) Zheng, Y.; Petersen, A. S.; Wan, H.; Hübner, R.; Zhang, J.; Wang, J.; Qi, H.; Ye, Y.; Liang, C.; Yang, J.; Cui, Z.; Meng, Y.; Zheng, Z.; Rossmeisl, J.; Liu, W. Scalable and Controllable Synthesis of Pt-Ni Bunched-Nanocages Aerogels as Efficient Electrocatalysts for Oxygen Reduction Reaction. *Adv. Energy Mater.* **2023**, *13*, 2204257.

(38) Deshpande, S.; Greeley, J. First-Principles Analysis of Coverage, Ensemble, and Solvation Effects on Selectivity Trends in NO Electroreduction on Pt_3Sn Alloys. *ACS Catal.* **2020**, *10*, 9320−9327.

(39) Yao, Y.; Huang, Z.; Xie, P.; Lacey, S. D.; Jacob, R. J.; Xie, H.; Chen, F.; Nie, A.; Pu, T.; Rehwoldt, M.; Yu, D.; Zachariah, M. R.; Wang, C.; Shahbazian-Yassar, R.; Li, J.; Hu, L. Carbothermal Shock Synthesis of High-Entropy-Alloy Nanoparticles. *Science* **2018**, *359*, 1489−1494.

(40) Kaiser, S. K.; Fako, E.; Surin, I.; Krumeich, F.; Kondratenko, V. A.; Kondratenko, E. V.; Clark, A. H.; López, N.; Pérez-Ramírez, J. Performance Descriptors of Nanostructured Metal Catalysts for Acetylene Hydrochlorination. *Nat. Nanotechnol.* **2022**, *17*, 606−612.

(41) Kusada, K.; Kobayashi, H.; Yamamoto, T.; Matsumura, S.; Sumi, N.; Sato, K.; Nagaoka, K.; Kubota, Y.; Kitagawa, H. Discovery of Face-Centered-Cubic Ruthenium Nanoparticles: Facile Size-Controlled Synthesis Using the Chemical Reduction Method. *J. Am. Chem. Soc.* **2013**, *135*, 5493−5496.

(42) Zhang, Q.; Kusada, K.; Wu, D.; Yamamoto, T.; Toriyama, T.; Matsumura, S.; Kawaguchi, S.; Kubota, Y.; Kitagawa, H. Selective Control of Fcc and Hcp Crystal Structures in Au-Ru Solid-Solution Alloy Nanoparticles. *Nat. Commun.* **2018**, *9*, 510.

(43) Zei, M. S. Epitaxial Growth of Ru and Pt on Pt(111) and Ru(0001), Respectively: A Combined AES and RHEED Study. *J. Nanotechnol.* **2010**, *2010*, No. 487193.

(44) Chen, P. C.; Liu, M.; Du, J. S.; Meckes, B.; Wang, S.; Lin, H.; Dravid, V. P.; Wolverton, C.; Mirkin, C. A. Interface and Heterostructure Design in Polyelemental Nanoparticles. *Science* **2019**, *363*, 959−964.

(45) Yao, Q.; Yu, Z.; Li, L.; Huang, X. Strain and Surface Engineering of Multicomponent Metallic Nanomaterials with Unconventional Phases. *Chem. Rev.* **2023**, *123*, 9676−9717.

(46) Kwon, S. G.; Krylova, G.; Phillips, P. J.; Klie, R. F.; Chattopadhyay, S.; Shibata, T.; Bunel, E. E.; Liu, Y.; Prakapenka, V. B.; Lee, B.; Shevchenko, E. V. Heterogeneous Nucleation and Shape Transformation of Multicomponent Metallic Nanostructures. *Nat. Mater.* **2015**, *14*, 215−223.

(47) Ha, M.; Kim, J. H.; You, M.; Li, Q.; Fan, C.; Nam, J. M. Multicomponent Plasmonic Nanoparticles: From Heterostructured Nanoparticles to Colloidal Composite Nanostructures. *Chem. Rev.* **2019**, *119*, 12208−12278.

(48) Lin, M.; Kim, G. H.; Kim, J. H.; Oh, J. W.; Nam, J. M. Transformative Heterointerface Evolution and Plasmonic Tuning of Anisotropic Trimetallic Nanoparticles. *J. Am. Chem. Soc.* **2017**, *139*, 10180−10183.

(49) Higgins, K.; Ziatdinov, M.; Kalinin, S. V.; Ahmadi, M. High-Throughput Study of Antisolvents on the Stability of Multicomponent Metal Halide Perovskites through Robotics-Based Synthesis and Machine Learning Approaches. *J. Am. Chem. Soc.* **2021**, *143*, 19945−19955.

(50) Zhao, R.; Dong, X.; Liang, P.; Li, H.; Zhang, T.; Zhou, W.; Wang, B.; Yang, Z.; Wang, X.; Wang, L.; Sun, Z.; Bu, F.; Zhao, Z.; Li, W.; Zhao, D.; Chao, D. Prioritizing Hetero-Metallic Interfaces via Thermodynamics Inertia and Kinetics Zincophilia Metrics for Tough Zn-Based Aqueous Batteries. *Adv. Mater.* **2023**, *35*, 2209288.

(51) Chen, S.; Aitken, Z. H.; Pattamatta, S.; Wu, Z.; Yu, Z. G.; Banerjee, R.; Srolovitz, D. J.; Liaw, P. K.; Zhang, Y.-W. Chemical-affinity disparity and exclusivity drive atomic segregation, short-range ordering, and cluster formation in high-entropy alloys. *Acta Mater.* **2021**, *206*, No. 116638.